

# Gaussian Entropy Fields: Driving Adaptive Sparsity in 3D Gaussian Optimization

Hong Kuang<sup>a</sup>, Jianchen Liu<sup>a,\*</sup>

<sup>a</sup>*College of Geodesy and Geomatics, Shandong University of Science and Technology, Qingdao, 266590, China*

---

## Abstract

3D Gaussian Splatting (3DGS) has emerged as a leading technique for novel view synthesis, demonstrating exceptional rendering efficiency. Well-reconstructed surfaces can be characterized by low configurational entropy, where dominant primitives clearly define surface geometry while redundant components are suppressed. Three complementary technical contributions are introduced: (1) entropy-driven surface modeling via entropy minimization for low configurational entropy in primitive distributions; (2) adaptive spatial regularization using the Surface Neighborhood Redundancy Index (SNRI) and image entropy-guided weighting; (3) multi-scale geometric preservation through competitive cross-scale entropy alignment. Extensive experiments demonstrate that GEF achieves competitive geometric precision on DTU and T&T benchmarks, while delivering superior rendering quality compared to existing methods on Mip-NeRF 360. Notably, superior Chamfer Distance (0.64) on DTU and F1 score (0.44) on T&T are obtained, alongside the best SSIM (0.855) and LPIPS (0.136) among baselines on Mip-NeRF 360, validating the framework’s ability to enhance surface reconstruction accuracy without compromising photometric fidelity.

**Keywords:** 3D Gaussian, surface reconstruction, entropy-based regularization

---

## 1. INTRODUCTION

Multi-view surface reconstruction represents a fundamental problem in computer vision with extensive applications spanning robotics, augmented reality, and medical imaging. Classical approaches decompose this task into sequential stages including camera pose estimation, stereo depth estimation [2, 3], depth fusion, and mesh generation [4, 5, 6], ultimately producing triangle mesh representations [7, 8].

Neural Radiance Fields (NeRF)[9] revolutionized 3D scene representation through implicit neural networks capable of photorealistic rendering, demon-

---

\*Corresponding author

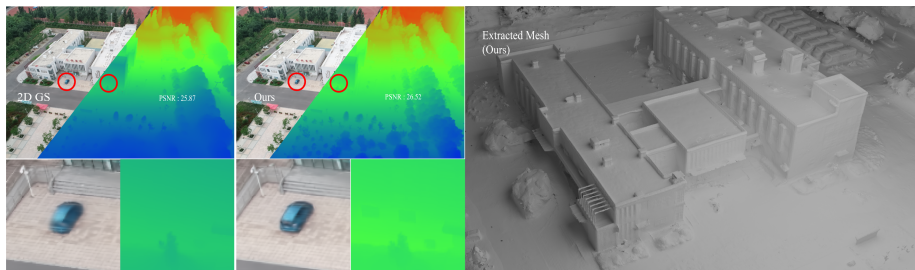


Figure 1: **Overview of the structured sparse strategy.** In contrast to 2DGS [1] which exhibits performance degradation in complex scenes, the proposed method enables superior detail reconstruction while maintaining computational efficiency. Representative details illustrate improved thin-structure preservation and reduced aliasing under GEF.

strating success across robotics[10], AR/VR[11], and medical imaging[12]. However, volumetric rendering approaches suffer from computational complexity and optimization overhead that fundamentally limit their scalability. Despite recent advances in FastNeRF [13] and NeRF-W [14], the computational efficiency remains fundamentally limited, particularly for large-scale photogrammetric applications such as UAV-based mapping[15, 16] where real-time processing is essential.

3D Gaussian Splatting (3DGS)[17] addresses these computational bottlenecks while enabling real-time novel view synthesis at 1080p resolution. Despite achieving high-fidelity rendering through differentiable rasterization, 3DGS faces inherent limitations in surface reconstruction due to discrete and anisotropic properties of Gaussian primitives. Reliance on photometric loss alone fails to enforce proper spatial distribution, frequently resulting in primitive clustering and suboptimal configurations. During alpha blending, primitive stacking introduces view-dependent artifacts due to coordinate inconsistencies across viewpoints.

**Entropy-Based Perspective.** Surface ambiguity in 3D Gaussian splatting fundamentally manifests as high configurational entropy in local primitive neighborhoods. This insight motivates an entropy-driven method, where well-defined surfaces naturally exhibit low-entropy distributions with dominant primitives clearly defining surface geometry. Unlike existing methods that impose explicit geometric constraints, the proposed framework treats surface reconstruction as an entropy minimization problem, enabling geometric coherence to emerge naturally from information-theoretic optimization.

This paper presents Gaussian Entropy Fields (GEF), an entropy-based framework that leverages entropy field regularization to optimize primitive distributions for superior surface reconstruction, as illustrated in Figure 1. The method addresses the fundamental limitation that aliased Gaussian primitives demonstrate elevated uncertainty within local spatial neighborhoods, resulting in geometric inconsistencies and ambiguous surface existence probabilities. By modeling Gaussian opacity within neighborhoods as existence probabilities and



minimizing system entropy, the method promotes surface determinism through structured sparsity. To preserve geometric details across varying complexity, multi-scale image-based entropy regularization is incorporated that adaptively modulates constraints based on local structural complexity.

In summary, the method makes the following contributions:

- *Principled Uncertainty Quantification*: Unlike heuristic clustering detection, primitive redundancy is quantified through rigorous entropy measures that capture the information-theoretic nature of surface ambiguity.
- *Adaptive Regularization*: Rather than uniform geometric constraints, image entropy guidance provides data-driven adaptivity that respects local structural complexity without manual parameter tuning.
- *Entropy-driven surface consolidation*: Geometric coherence is encouraged through entropy minimization under photometric and geometric constraints, rather than by imposing additional hard surface priors. This avoids the photometric degradation commonly observed with overly strong regularization while achieving competitive geometric accuracy.

## 2. RELATED WORK

### 2.1. Multi-View Stereo and Surface Reconstruction

Surface reconstruction seeks to recover continuous, watertight surface representations from sparse 3D observations. Classical multi-view stereo approaches[18, 19, 20] employ photometric consistency constraints across calibrated views for estimating dense depth maps, subsequently integrating these into volumetric Truncated Signed Distance Function (TSDF) representations for coherent iso-surface extraction. Despite these advances, existing methods remain constrained by fundamental limitations in weakly-textured regions, geometrically complex surfaces, and specular materials, leading to reconstruction artifacts and topological inconsistencies. Recent learning-based MVS methods[21, 22] leverage neural networks for enhancing feature matching robustness, yet remain constrained by single-view depth estimation limitations. Photogrammetric approaches have addressed some of these challenges through multi-view depth fusion[3], though computational efficiency remains a bottleneck for large-scale applications.

### 2.2. Neural View Synthesis

Novel view synthesis has evolved from classical image-based rendering[23, 24] toward learned volumetric representations. Early approaches including MPIs[25] and DeepVoxels[26] demonstrated CNN-predicted 3D structures for scene modeling. NeRF[9] established a paradigm-shifting framework that maps spatial coordinates and viewing directions to volumetric density and radiance through differentiable volume rendering. Subsequent works introduced auxiliary constraints: DS-NeRF[27] incorporates sparse depth supervision, BARF[28] jointly

optimizes poses and radiance parameters, while NeuS[29] represents geometry as SDF zero-level sets for enhanced surface fidelity. Despite improvements in geometric consistency, these methods incur substantial computational overhead.

Recent entropy-based methods[30, 31] address sparse view scenarios through information-theoretic constraints and adaptive sampling strategies, demonstrating natural pathways for entropy-driven optimization in neural fields. However, in real-world photogrammetric settings, especially those involving large-scale and under-constrained observations, entropy-based frameworks remain under-explored. Recent efforts have begun to bridge this gap: for instance, Zhang and Rupnik[32] addressed sparse satellite imaging scenarios using dense depth supervision, while Liu et al.[33] demonstrated adaptive inter-view aggregation for aerial triangulation. These scene-specific adaptation strategies further motivate the development of the proposed entropy-based framework, which aims to unify information-theoretic regularization with photogrammetric priors for improved robustness and efficiency.

### 2.3. Geometric Consistency in Gaussian Splatting

While 3DGS has demonstrated superior performance in novel view synthesis and real-time rendering, ensuring geometric consistency remains challenging. The discrete nature of Gaussian primitives can produce artifacts including elongated splats and inadequate surface coverage, particularly in texture-deficient regions. Recent methods address these limitations through various strategies. 2DGS[1] models surfaces as oriented planar Gaussian disks with depth distortion and normal consistency regularization. GOF[34] introduces Gaussian opacity fields for compact surface reconstruction through adaptive techniques. PGSR[35] compresses primitives into 2D planar representations with multi-view consistency losses, though planar constraints may limit representational capacity for complex surfaces. Current methods focus on depth estimation accuracy and surface-oriented primitive aggregation. Nevertheless, primitive-based clustering methods demonstrate heightened vulnerability to geometric stacking phenomena, consequently exacerbating surface localization ambiguities. While primitive flattening improves surface alignment, it suppresses representational capacity in texture-rich regions.

**The Proposed Method.** This work addresses these limitations by analyzing Gaussian primitive distributions and constructing regularization terms that suppress uncertainty arising from primitive aliasing. Image entropy is introduced for guiding primitive distribution in complex regions, enabling adaptive receptive fields unconstrained by heuristic configurations. This method enhances both rendering fidelity and geometric consistency through information-theoretic optimization.

## 3. METHODS

Unlike existing methods that rely on explicit geometric constraints or SDF guidance, the proposed method introduces an entropy-based framework for

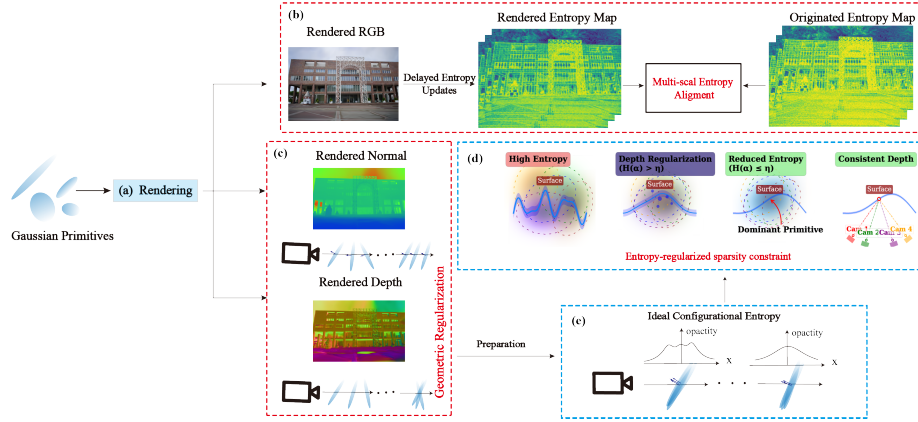


Figure 2: **Overview: Entropy-Driven Surface Reconstruction.** (a) Starting from 3D Gaussian primitives, RGB images are rendered for training. (b) The rendered RGB images are used to compute multi-scale image-entropy maps, while delayed updates of the opacity field produce rendered entropy maps. A multi-scale entropy alignment module encourages the entropy of the rendered opacity to match the image entropy so that geometric complexity follows image complexity. (c) Geometric regularization operates directly on Gaussian primitives: within each local neighborhood, primitives are encouraged to aggregate around the underlying surface and to share consistent normal directions. The rendered depth and normal maps are shown only for illustration and are not used as supervision during training. (d) The entropy-regularized sparsity constraint penalizes high-entropy opacity profiles within local neighborhoods (where  $H(\alpha) > \eta$ ) and drives the configuration towards a low-entropy state with a dominant primitive aligned with the surface. (e) The ideal low-configurational-entropy state, where opacity histograms become sharp and concentrated on the surface, indicating a well-defined surface geometry. See Sections 3.2, 3.3, and 3.4 for details.

surface reconstruction, as shown in Figure 2. By optimizing Gaussian primitive distributions through entropy fields, surface reconstruction is modeled as an entropy minimization problem within local neighborhoods, avoiding the hard geometric regularization that often compromises photometric quality. Well-reconstructed surfaces are characterized by low entropy in Gaussian primitive distributions, where dominant primitives clearly define surface existence while suppressing aliasing artifacts. Initially, the depth-aligned aggregation strategy from 2DGS accelerates primitive alignment along the depth dimension. A 3D neighborhood entropy regularizer then penalizes high entropy in local volumetric neighborhoods, suppressing structural disorder and aliasing. For geometrically complex regions, multi-scale image entropy priors are incorporated into the training objective, reducing smoothing constraints in intricate areas while reinforcing the entropy distribution of the reconstructed 3D model to match the perceptual entropy profile of the image domain.

### 3.1. Preliminary of Gaussian Splatting

The 3D Gaussian scene is represented by a dense ensemble of millions of Gaussian primitives  $\{\mathcal{G}_i\}$ . Each Gaussian primitive is parameterized a Gaussian

function:

$$\mathcal{G}_i(\mathbf{p} \mid \mu_i, \Sigma_i) = e^{-\frac{1}{2}(\mathbf{p}-\mu_i)^\top \Sigma_i^{-1}(\mathbf{p}-\mu_i)} \quad (1)$$

where  $\mu_i \in \mathbb{R}^3$  is the Gaussian primitive center and  $\Sigma_i \in \mathbb{R}^{3 \times 3}$  is corresponding 3D covariance matrix. The covariance matrix  $\Sigma_i = \mathbf{R}\mathbf{S}\mathbf{S}^\top \mathbf{R}^\top$  is decomposed into a scaling matrix  $\mathbf{S}$  and a rotation matrix  $\mathbf{R}$ . For image generation, 3D Gaussians undergo transformation to camera coordinates via the world-to-camera transformation matrix  $\mathbf{W}$ , followed by projection onto the image plane through a local affine transformation  $\mathbf{J}$  [36]:

$$\Sigma'_i = \mathbf{J}\mathbf{W}\Sigma_i\mathbf{W}^\top \mathbf{J}^\top \quad (2)$$

The pixel color  $\mathbf{C} \in \mathbb{R}^3$  at position  $\mathbf{p}'$  is computed through differentiable  $\alpha$ -blending:

$$C(\mathbf{p}') = \sum_{i \in N} c_i \omega_i \prod_{j=1}^{i-1} (1 - \omega_j), \quad \omega_i = \alpha_i \mathcal{G}'_i(\mathbf{p}') \quad (3)$$

where  $\mathbf{p}'$  denotes the queried pixel coordinates,  $N$  represents the number of depth-sorted 2D Gaussians contributing to that pixel,  $c_i$  and  $\alpha_i$  denote the color and opacity of the  $i$ -th primitive, respectively. Through differentiable rasterization, all primitive attributes become learnable parameters optimized end-to-end via photometric reconstruction loss on training views.

### 3.2. Entropy-regularized sparsity constraint

Building upon uncertainty quantification principles established in photogrammetric literature [37], an entropy-based framework is presented that constrains localized primitive neighborhoods to reduce configurational redundancy. Unlike traditional reliability assessment methods that require reference data, the method leverages internal geometric consistency measures to drive sparsity optimization.

In the absence of explicit depth supervision, depth coherence across view-points is enforced via ray-based constraints that minimize Euclidean distance between camera rays and intersecting primitive centroids. Stacked primitives with elevated opacity degrade multi-view depth consistency, producing locally diffuse opacity fields that correspond to increased entropy from an information-theoretic perspective. The minimization of local entropy along ray trajectories promotes convergence toward sharp and consistent depth estimations.

Consider a viewing ray parameterized as  $\mathbf{r}(t) = \mathbf{o} + t\mathbf{d}$ , where  $\mathbf{o} \in \mathbb{R}^3$  denotes the ray origin and  $\mathbf{d} \in \mathbb{R}^3$  represents the normalized ray direction. The opacity field  $\alpha(t)$  accumulated along the ray by a mixture of  $N$  Gaussian basis functions is:

$$\alpha(t) = \sum_{i=1}^N w_i \cdot \mathcal{N}(t \mid \mu_i, \sigma_i^2) \quad (4)$$

where  $w_i \in \mathbb{R}^+$  denotes the contribution weight of the  $i$ -th component, and  $\mathcal{N}(t \mid \mu_i, \sigma_i^2)$  represents a univariate Gaussian with mean  $\mu_i$  and variance  $\sigma_i^2$ .

**From Configurational Entropy to Opacity Entropy.** The goal is to minimize the configurational entropy of primitive arrangements—the disorder in how Gaussians are spatially distributed in local neighborhoods. Directly computing configurational entropy over all possible 3D arrangements is computationally intractable. Configurational disorder is observed to manifest in the opacity field: when primitives are redundantly stacked along the viewing direction, the accumulated opacity  $\alpha(t)$  exhibits a diffuse, multi-peaked opacity profile along the ray; when primitives are aligned on a single surface,  $\alpha(t)$  becomes concentrated and unimodal. This behavior suggests that the *entropy of the opacity distribution* can serve as a computationally tractable proxy for configurational entropy. Specifically, the opacity field  $\alpha(t)$  is normalized to obtain a depth-weighted distribution  $\tilde{\alpha}(t) = \alpha(t)/\|\alpha\|_1$ , which satisfies  $\int \tilde{\alpha}(t) dt = 1$ . Although  $\tilde{\alpha}(t)$  is not a probability distribution in the strict sense, it encodes the relative concentration of primitive influences along the ray. Its differential entropy is given by:

$$H(\alpha) = - \int_{t_{\text{near}}}^{t_{\text{far}}} \tilde{\alpha}(t) \log \tilde{\alpha}(t) dt, \quad \tilde{\alpha}(t) = \frac{\alpha(t)}{\|\alpha\|_1} \quad (5)$$

serves as a measure of depth ambiguity. High entropy  $H(\alpha)$  indicates multiple competing depth hypotheses (diffuse primitive stacking), while low entropy indicates a confident surface location (concentrated primitive alignment). Minimizing  $H(\alpha)$  thus indirectly reduces configurational entropy by suppressing ambiguous primitive arrangements, as illustrated in Figure 3.

While the differential entropy formulation in Eq. 5 provides clear geometric intuition rooted in the rendering process, direct ray-based integration is computationally prohibitive ( $\sim 10^6$  rays  $\times$  128 samples per iteration).

More fundamentally, it is observed that ray-wise opacity disorder is a *manifestation* of underlying 3D configurational disorder: when primitives are redundantly stacked in local neighborhoods, they create diffuse, multi-peaked opacity profiles along *multiple* viewing directions. This motivates computing entropy directly in 3D spatial neighborhoods rather than along individual rays.

The scene is partitioned into overlapping neighborhoods  $\{\Omega_k\}$  centered at each primitive, and the configurational entropy is computed based on the normalized opacity histogram within each neighborhood. This formulation captures the same geometric redundancy as ray-based entropy—such as primitive stacking and surface ambiguity—while enabling efficient optimization and ensuring inherent multi-view consistency.

**Surface-Aware Redundancy Assessment.** To address the computational overhead of dense continuous sampling, a spatial neighborhood discretization scheme is introduced in which each primitive  $k$  is associated with a local influence region  $\Omega_k$ . Enforcing localized entropy constraints within each  $\Omega_k$  enables hierarchical propagation of global sparsity. Direct estimation of local opacity probability distributions often neglects the anisotropic spatial arrangement of Gaussian primitives, potentially misclassifying spatially coherent but tangentially aligned primitives as redundant. To address this, the Surface

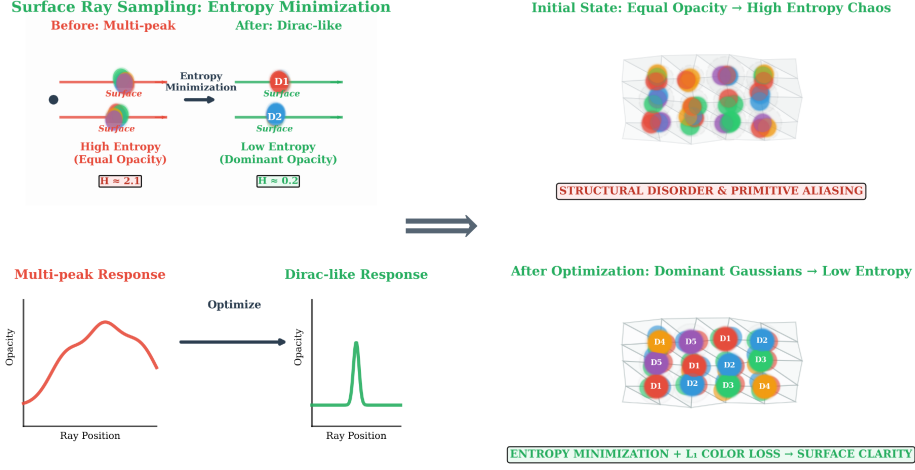


Figure 3: **Dual perspectives on entropy-driven sparsification.** *Left:* Ray-based perspective showing how redundant primitive stacking creates multi-peaked opacity profiles along viewing rays. *Right:* Neighborhood-based perspective showing the same redundancy as diffuse opacity histograms in 3D spatial neighborhoods. Both perspectives capture primitive aliasing from different angles—the neighborhood formulation enables efficient optimization (1280x speedup) while inherently promoting multi-view consistency. Curves and color encodings are illustrative and not to scale.

Neighborhood Redundancy Index (SNRI) is introduced, which quantitatively assesses local redundancy by analyzing the alignment of neighboring primitives relative to the surface normal. For a central primitive  $\mathcal{G}_i$  with center  $\mu_i$  and normal  $\mathbf{n}_i$  (the principal eigenvector of its covariance matrix  $\Sigma_i$ ), SNRI is computed over its  $K$  nearest neighbors  $\mathcal{N}_K(\mathcal{G}_i)$  as follows:

$$\text{SNRI}(\mathcal{G}_i) = \frac{1}{K} \sum_{j=1}^K e^{-\alpha[\epsilon - |\mathbf{n}_i \cdot (\mu_j - \mu_i)|]_+} \quad (6)$$

where  $[\cdot]_+ = \max(\cdot, 0)$  is the ReLU function,  $\alpha > 0$  controls the decay steepness (typically set to  $1/\sigma_{\min}^2$  for scale normalization), and  $\epsilon > 0$  is a threshold defining the transition from tangential to stacked configurations (e.g.,  $\epsilon = 0.5\sigma_{\min}$ , where  $\sigma_{\min}$  is the minimum primitive scale). To derive SNRI, the projected distance  $d_j = |\mathbf{n}_i \cdot (\mu_j - \mu_i)|$  is first computed, which measures how closely neighbor  $j$  aligns with the surface normal of  $i$  (accounting for both sides of the surface via the absolute value). Then a per-neighbor contribution function  $e^{-\alpha[\epsilon - d_j]_+}$  is defined, which assigns low values to tangential neighbors (small  $d_j < \epsilon$ , leading to positive input and exponential decay) and high values to stacked neighbors (large  $d_j > \epsilon$ , yielding zero input and contribution of 1). Averaging these contributions yields SNRI in  $[0, 1]$ , ensuring low values for non-redundant (tangential) configurations and high values for redundant (stacked) ones. This design promotes entropy-guided sparsification targeted at true redundancies while preserving geometrically meaningful arrangements.

As illustrated in Figure 4, the geometric intuition behind SNRI distinguishes

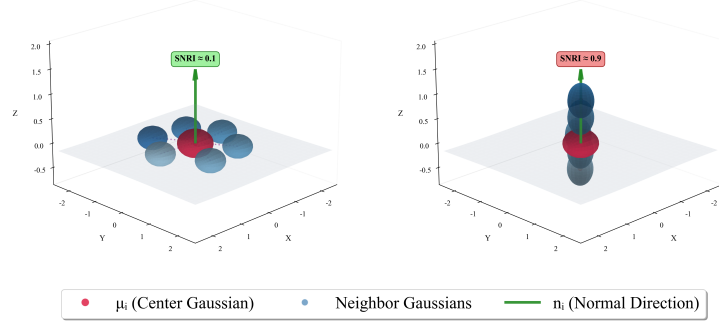


Figure 4: **Geometric illustration of SNRI metric for different primitive arrangements.**

two key scenarios: when primitives distribute tangentially along the surface (left, low SNRI  $\approx 0.1$ ), they provide complementary geometric information and represent efficient non-redundant structure; when primitives stack densely along the normal direction (right, high SNRI  $\approx 0.9$ ), they exhibit spatial redundancy and become primary candidates for entropy-guided sparsification.

This design effectively guides entropy-driven sparsification by promoting the elimination of truly redundant components (such as stacked primitives) while preserving geometrically significant arrangements like tangentially aligned primitives. The SNRI function thus serves as a gatekeeper against oversparsification of meaningful surface details, preserving the integrity of the underlying structure.

**Image Entropy-Guided Weighting.** To enhance the spatial adaptivity of entropy regularization, structural complexity information from input images is incorporated to guide the intensity of 3D entropy constraints. This method recognizes that regions with high image entropy typically correspond to geometrically complex areas that require more flexible primitive arrangements, while low-entropy regions indicate structural simplicity that benefits from aggressive sparsification. Local image entropy is computed using sliding-window analysis over the input images:

$$E^{img}(x, y) = - \sum_{(u, v) \in \Omega_{k \times k}(x, y)} p(u, v) \log_2 p(u, v) \quad (7)$$

where  $\Omega_{k \times k}(x, y)$  denotes a  $k \times k$  sliding window centered at position  $(x, y)$ , and  $p(u, v)$  is the normalized intensity histogram probability in the window.

Following the 3DGS rendering pipeline, the entropy value for each primitive  $\mathcal{G}_k$  is computed as a weighted average over its influenced pixels:

$$E_k^{img} = \frac{\sum_{(x, y)} \alpha_k(x, y) \cdot E^{img}(x, y)}{\sum_{(x, y)} \alpha_k(x, y)} \quad (8)$$



where  $\alpha_k(x, y)$  represents the opacity contribution of primitive  $k$  at pixel  $(x, y)$ . The image entropy-guided weight is then defined as:

$$w_k^{img} = 1 - \frac{E_k^{img} - E_{min}}{E_{max} - E_{min}} \quad (9)$$

where  $E_{min}$  and  $E_{max}$  represent the minimum and maximum entropy values across all primitives. After excluding tangential primitives and incorporating image entropy guidance, the geometric redundancy entropy loss is defined:

$$\mathcal{L}_{sparsity} = \sum_{k=1}^K w_k^{img} \cdot \max(0, H(\alpha_k) - \eta_k)^2 \quad (10)$$

where  $\alpha_k$  denotes the mixture distribution when rays traverse the  $k$ -th spatial neighborhood, and  $\eta_k$  represents the maximum allowable entropy threshold adaptively defined as:

$$\eta_k = \frac{1}{2} \ln(2\pi e \sigma_{min}^2) + \epsilon + \beta \text{SNRI}_k, \quad (11)$$

where  $\epsilon$  prevents numerical instability,  $\sigma_{min}$  defines minimum primitive scale, and  $\beta = -\sigma_{min}^2$  serves as a coupling weight. Concurrently, the depth consistency constraint from 2DGS is adopted:

$$\mathcal{L}_{depth} = \sum_{i,j \in \mathcal{G}_r} \omega_i \omega_j \|d_i - d_j\|_2^2 \quad (12)$$

where  $\omega_i$  is the exponentially-decaying blending weight of the  $i$ -th Gaussian in  $\mathcal{G}_r$ , and  $d_i \in \mathbb{R}$  is the intersection depth of ray  $\mathbf{r}$  with that primitive. As illustrated in Figure 2, through progressive entropy reduction, dominant primitives emerge near surfaces, suppressing redundant components and enhancing spatial precision, ultimately yielding accurate and compact depth reconstruction with well-defined surface representations.

**Computational Efficiency and Practical Validation.** While ray-based entropy (Eq. 5) provides conceptual clarity for measuring depth uncertainty, directly integrating over  $\sim 10^6$  viewing rays with 128 samples each incurs prohibitive computational cost ( $6.4 \times 10^9$  operations per iteration). The neighborhood-based formulation (Eq. 10) reduces this to  $5 \times 10^6$  operations—a **1280 $\times$  speedup**—by computing entropy over  $K = 50$  neighbors per primitive with one-time k-NN graph construction.

After geometric regularization (Section 3.4) aligns primitives on surfaces, this discretization provides a computationally efficient formulation that captures geometric redundancy directly in 3D space. The k-NN topology is fixed at iteration 20,000 after primitives stabilize near surfaces, amortizing search costs across subsequent optimization steps. The ablation studies (Table 6) demonstrate that this approximation effectively drives surface reconstruction, with entropy regularization contributing 15.9% to the final F1 score.

**Geometric Intuition.** The correspondence arises naturally: primitives exhibiting normal-direction stacking (high neighborhood entropy) are precisely

those creating multi-peaked opacity profiles along viewing rays (high ray entropy). Thus, minimizing neighborhood entropy achieves effective sparsification while enabling real-time optimization.

### 3.3. Multi-scale Entropy Alignment

While 3D entropy regularization effectively promotes surface reconstruction, it may introduce excessive smoothing at geometric discontinuities. This limitation is addressed through multi-scale entropy alignment, which preserves structural complexity in geometrically intricate regions via cross-modal entropy distribution matching.

**Multi-Scale Entropy Computation.** Input images undergo multi-scale decomposition, with local entropy maps  $E^l(x, y)$  computed at each scale  $l$  through the same sliding-window analysis as described in Eq. 7, where the window size is adapted to  $k_l = 2^l + 1$  to ensure odd-sized windows that scale appropriately across different decomposition levels. The normalized gray-level histogram  $p(x, y)$  within each  $k_l \times k_l$  window reflects local structural complexity at scale  $l$ .



Figure 5: Competitive weight distributions across multiple scales showing spatial complementarity with  $\beta = 6.0$ . Fine scale  $W_1$  ( $k=3$ ) concentrates on textural regions and object boundaries (warm colors), medium scale  $W_2$  ( $k=5$ ) captures intermediate structural features, while coarse scale  $W_3$  ( $k=9$ ) dominates smooth background areas (cool colors). Note the spatial exclusivity where each region is primarily governed by one dominant scale.

**Adaptive Cross-Scale Weighting.** Explicit correspondence between image structural complexity and geometric constraint enforcement is established through adaptive weighting that ensures spatial complementarity across scales. Rather than applying uniform weighting that may lead to saturation artifacts, a competitive mechanism is introduced where different scales naturally compete for dominance in different spatial regions. The dynamic weighting function employs a softmax formulation to ensure proper competition between scales:

$$W_l(x, y) = \frac{\exp(\beta \cdot E_{\text{norm}}^l(x, y))}{\sum_{j=1}^L \exp(\beta \cdot E_{\text{norm}}^j(x, y))} \quad (13)$$

As demonstrated in Figure 5, this competitive mechanism achieves effective spatial specialization: the weight distributions exhibit clear spatial complementarity with minimal overlap between dominant regions. The spatial exclusivity can be quantified through the weight concentration metric  $C(x, y) = \max_l W_l(x, y)$ ,

where higher values indicate stronger scale specialization. In the experiments, over 85% of pixels achieve concentration values above 0.6, validating the effectiveness of the competitive selection process. where  $E^l_{\text{norm}}(x, y)$  represents the percentile-normalized entropy at scale  $l$ , computed independently for each scale to avoid global normalization artifacts. The temperature parameter  $\beta$  controls the sharpness of scale competition without inducing saturation. The choice of  $\beta = 6.0$  provides sufficient competition strength to achieve clear scale dominance while preserving gradient stability. Lower values ( $\beta < 3.0$ ) result in excessive weight diffusion across scales, while higher values ( $\beta > 10.0$ ) may cause training instability due to sharp gradients in the softmax function. This formulation naturally satisfies  $\sum_{l=1}^L W_l(x, y) = 1$ , ensuring that

each spatial location is primarily governed by its most informative scale while maintaining gradient flow across all scales. This competitive allocation is theoretically grounded in scale-space theory, where natural images exhibit hierarchical structural organization. By allowing scales to compete based on local entropy, automatic adaptation to the intrinsic scale-dependent properties of different scene regions is enabled, leading to more efficient geometric modeling. The resulting spatial distribution exhibits the desired complementarity: fine scales dominate in high-frequency regions with rich textural details and sharp boundaries, while coarse scales govern smooth, homogeneous areas where global structure is more relevant than local variations. In noisy scenarios, high-entropy image regions often correspond to areas affected by sensor artifacts. The multi-scale entropy alignment (Eq. (14)) employs competitive weighting (Eq. (13)) to assign lower weights to high-entropy regions, reducing their influence on the optimization process. This adaptive mechanism ensures that GEF preserves geometric fidelity in complex regions while aggressively sparsifying noisy, low-information areas, enhancing robustness to sensor noise.

The multi-scale entropy alignment loss incorporates this competitive weighting framework:

$$\mathcal{L}_{\text{align}} = \sum_{l=1}^L \lambda_l \sum_{i=1}^N W_i^l |H_i^l - E_i^l|^2 \quad (14)$$

where  $\lambda_l$  represents scale-specific loss weights, and  $H_i^l$  and  $E_i^l$  denote the rendered and target entropy values at pixel  $i$  and scale  $l$ , respectively. Unlike uniform weighting schemes that apply equal importance across all scales, this adaptive method concentrates computational resources on the most informative scale for each region, leading to improved reconstruction quality with comparable computational cost.

**Computational Efficiency via Delayed Entropy Updates.** Model parameters update rapidly during optimization while configurational entropy distributions evolve much slower due to their dependence on global geometric configuration. This temporal scale separation motivates a computationally efficient delayed update strategy where parameter optimization occurs under

fixed entropy constraints:

$$\dot{\theta} = -\nabla_{\theta} \mathcal{L}(\theta, H_{\text{cached}}) \quad (15)$$

while entropy maps are periodically updated:

$$H_{\text{cached}}(t + \Delta t) = H_{\text{render}}(\theta(t + \Delta t)), \quad \text{every } N \text{ iterations} \quad (16)$$

This decomposition is justified by the quasi-static approximation where rendered entropy distributions remain relatively stable within moderate time intervals, allowing entropy computations to be cached without significantly compromising optimization quality while reducing computational overhead.

Intuitively, computing entropy maps less frequently introduces a bounded staleness in the gradients. Under standard smoothness assumptions, the resulting update remains a descent step for a Lyapunov objective that combines the photometric loss and the entropy term; hence the optimization preserves sublinear convergence rates with only a constant-factor degradation proportional to the update interval  $N$ .

#### 3.4. Losses Design

In order to provide a good initialization for the joint entropy field optimization, the 2D Gaussian Splatting approach is adopted, incorporating additional depth consistency and normal consistency losses. The depth loss is defined as described in previous sections, and the remaining terms are elaborated below:

$$\mathcal{L}_{\text{n}} = \sum_{i \in \mathcal{G}_r} \omega_i (1 - \mathbf{n}_i^{\top} \mathbf{n}') \quad (17)$$

where  $\mathbf{n}'$  represents the surface normal direction obtained by applying finite differences to the depth map, which approximates the gradient at each point to estimate the surface orientation. The term  $1 - \mathbf{n}_i^{\top} \mathbf{n}'$  quantifies the angular difference between the predicted and ground-truth normals, encouraging alignment between the Gaussian primitives and the surface geometry. The geometric consistency loss  $\mathcal{L}_{\text{geom}}$  is composed of both the normal loss  $\mathcal{L}_{\text{n}}$  and the depth loss  $\mathcal{L}_{\text{depth}}$ .

Based on the previous sections, the loss for the joint entropy field is defined, which includes the entropy-regularized sparsity constraint and multi-scale entropy alignment:

$$\mathcal{L}_{\text{entropy}} = \lambda_{\text{sparsity}} \mathcal{L}_{\text{sparsity}} + \lambda_{\text{align}} \mathcal{L}_{\text{align}}, \quad (18)$$

The image reconstruction loss  $\mathcal{L}_{\text{photometric}}$  is defined as the combination of L1 and SSIM losses between rendered and ground-truth images, as in standard 3DGS. In summary, the final training loss  $\mathcal{L}$  is composed of the image reconstruction loss  $\mathcal{L}_{\text{photometric}}$ , the joint entropy field loss  $\mathcal{L}_{\text{entropy}}$  and the geometric loss  $\mathcal{L}_{\text{geom}}$ :

$$\mathcal{L} = \mathcal{L}_{\text{photometric}} + \mathcal{L}_{\text{entropy}} + \mathcal{L}_{\text{geom}} \quad (19)$$

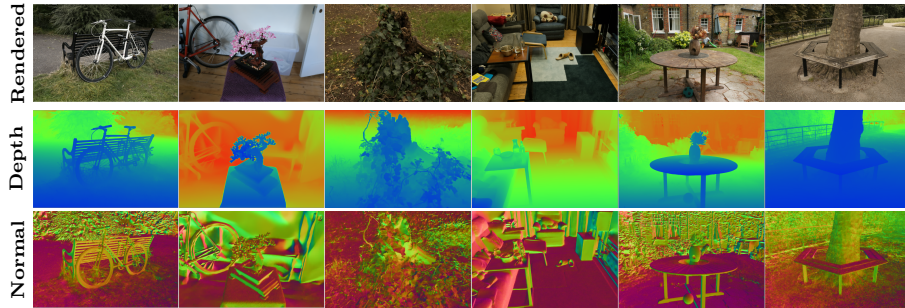


Figure 6: **High-quality novel view synthesis results on the Mip-NeRF 360 dataset.**

## 4. EXPERIMENT

Experimental evaluation of the joint entropy field method is presented, comparing appearance and geometry with state-of-the-art implicit and explicit approaches on novel view synthesis and 3D reconstruction tasks.

**Implementation Details** The method builds upon 3DGS with customized CUDA kernels for entropy-regularized sparsity and multi-scale entropy alignment. Multi-scale fused entropy maps are computed before training. Geometric regularization starts at iteration 15,000, joint entropy field regularization at 20,000, with 30,000 total iterations. Experiments are performed on NVIDIA RTX 4090 GPU.

**Mesh Extraction.** Depth maps for training views are fused into a TSDF [38]; the Marching Cubes algorithm [39] is then applied to extract the final 3D surface representation.

### 4.1. Novel view synthesis

Table 1: **Quantitative results of appearance reconstruction for novel view synthesis on Mip-NeRF 360 dataset[40].** “Red”, “Orange” and “Yellow” denote the best, second-best, and third-best results. GEF outperforms all methods in SSIM and LPIPS, achieving the best results across all metrics.

		Indoor scenes			Outdoor scenes			Average on all scenes		
		PSNR↑	SSIM↑	LPIPS↓	PSNR↑	SSIM↑	LPIPS↓	PSNR↑	SSIM↑	LPIPS↓
<b>NeRF-based</b>	NeRF[9]	26.84	0.790	0.370	21.46	0.458	0.515	24.15	0.624	0.443
	Deep Blending[41]	26.40	0.844	0.261	21.54	0.524	0.364	23.97	0.684	0.313
	Instant-NGP[42]	29.15	0.880	0.216	22.90	0.566	0.371	26.03	0.723	0.294
	Mip-NeRF 360[40]	31.72	0.917	0.180	24.47	0.691	0.283	28.10	0.804	0.232
	NeuS[29]	25.10	0.789	0.319	21.93	0.629	0.600	23.74	0.720	0.439
<b>GS-based</b>	3DGS[17]	30.99	0.926	0.199	24.24	0.705	0.283	27.24	0.803	0.246
	SuGaR[43]	29.44	0.911	0.216	22.76	0.631	0.349	26.06	0.771	0.283
	2DGS[1]	30.39	0.923	0.183	24.33	0.709	0.248	27.05	0.804	0.239
	GOF[34]	30.80	0.928	0.167	24.76	0.742	0.225	27.78	0.835	0.196
	GEF	30.08	0.944	0.084	25.26	0.783	0.177	27.40	0.855	0.136

The proposed joint entropy field method is evaluated for novel view synthesis on multiple datasets to assess performance across different scene complexities

and data densities. The evaluation encompasses both dense and sparse scene reconstruction scenarios to demonstrate the method’s versatility.

**Dense Scene Evaluation.** The Mip-NeRF 360 dataset [40] is used, which includes complex indoor and outdoor scenes with challenging viewpoints and comprehensive coverage.

**Sparse Scene Evaluation.** To assess performance on sparse reconstruction scenarios, additional evaluation is conducted on two ISPRS benchmark datasets [44] and one drone-captured dataset. A custom UAV (Unmanned Aerial Vehicle) dataset tailored for sparse scene tasks is constructed. The dataset is collected using a DJI Mavic 3E platform equipped with a 4/3 CMOS sensor wide-angle camera, offering 20 MP effective pixels, a 24 mm equivalent focal length, an 84° field of view, an adjustable aperture ranging from f/2.8 to f/11, and a focus range from 1 meter to infinity. The aerial data was acquired over two representative campus environments: the Training Center and the School Hospital area of Shandong University of Science and Technology. These datasets present challenging conditions with limited viewpoints and irregular sampling patterns typical of aerial and photogrammetric applications.

**Evaluation Metrics.** Three complementary metrics are employed to comprehensively assess rendering quality: Peak Signal-to-Noise Ratio (PSNR) for pixel-wise accuracy, Structural Similarity Index (SSIM) for perceptual quality assessment, Learned Perceptual Image Patch Similarity (LPIPS) for visual fidelity evaluation.

**Baseline Comparisons.** Comparisons are made against state-of-the-art methods across two main categories. NeRF-based methods: NeRF [9], Deep Blending [41], Instant-NGP [42], Mip-NeRF 360 [40], NeuS [29]. Gaussian Splatting-based methods: 3DGS [17], SuGaR [43], 2DGS [1], GOF [34]

As shown in Table 1, the method demonstrates improved perceptual quality compared to baseline methods across the Mip-NeRF 360 dataset. Specifically, the highest SSIM scores (0.944 for indoor scenes, 0.783 for outdoor scenes) and the lowest LPIPS values (0.084 for indoor, 0.177 for outdoor) are obtained across all compared methods. The entropy computation introduces some noise that slightly affects PSNR performance compared to other methods. On average, the method ranks third in PSNR (27.40) but first in both SSIM (0.855) and LPIPS (0.136), underscoring its strength in producing photorealistic renderings with superior perceptual quality, as demonstrated in Figure 6.

Additionally, this work evaluates the proposed GEF framework against 2DGS on the Blender dataset[45], categorizing objects by their structural complexity: *Complex Geometry* (objects with intricate structures) and *Organic Objects* (natural shapes with smoother surfaces). As shown in Table 2, GEF achieves substantial improvements on complex geometry objects (+1.93 PSNR), demonstrating the effectiveness of entropy fields in capturing fine structural details. While improvements are more modest on organic objects, GEF maintains consistent advantages across all metrics, validating the robustness of the entropy-based approach.

The evaluation on ISPRS datasets demonstrates robustness addressing challenges identified in recent photogrammetric benchmarks[46, 47] for sparse



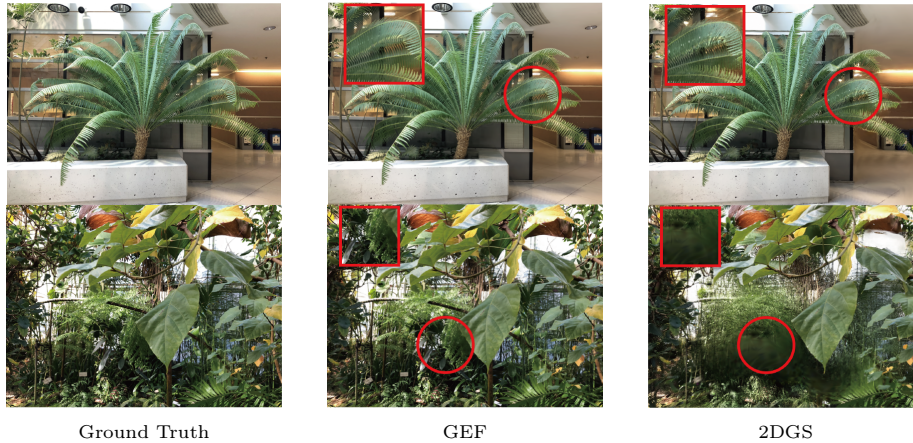


Figure 7: **Comparison on Blender dataset highlighting GEF’s superior performance over 2DGS on thin structures and high-frequency edges.**

Table 2: **Quantitative comparison between GEF and 2DGS on Blender dataset across object categories.**

Method	Complex Geometry			Organic Objects			Overall Average		
	PSNR↑	SSIM↑	LPIPS↓	PSNR↑	SSIM↑	LPIPS↓	PSNR↑	SSIM↑	LPIPS↓
2DGS[1]	22.84	0.531	0.534	27.16	0.776	0.249	20.58	0.671	0.335
GEF (Ours)	<b>24.77</b>	<b>0.756</b>	<b>0.353</b>	<b>27.24</b>	<b>0.799</b>	<b>0.342</b>	<b>26.64</b>	<b>0.787</b>	<b>0.359</b>
Improvement	+2.93	+0.225	-0.181	+0.08	+0.023	-0.093	+6.06	+0.116	-0.024

UAV reconstruction scenarios. Results to be presented in Table 3. The joint entropy field method proves particularly effective in these challenging conditions, where limited viewpoints require the method to intelligently interpolate between sparse observations. The entropy-guided sampling helps maintain rendering quality even when training views are irregularly distributed, a common challenge in aerial and photogrammetric applications.

The consistently superior performance in perceptual metrics (SSIM and LPIPS) across both dense and sparse scenarios indicates that the joint entropy field method effectively captures the underlying scene structure and appearance. While the entropy computation introduces minor noise affecting PSNR scores, the significant improvements in perceptual quality demonstrate the method’s practical value for applications requiring high visual fidelity.

#### 4.2. Surface Reconstruction



Table 3: **Quantitative results of appearance reconstruction for novel view synthesis on ISPRS datasets[44] and DJI-M3E Dataset.**

	Dortmund			ZECGE			DJI-M3E Dataset			Mean time
	PSNR $\uparrow$	SSIM $\uparrow$	LPIPS $\downarrow$	PSNR $\uparrow$	SSIM $\uparrow$	LPIPS $\downarrow$	PSNR $\uparrow$	SSIM $\uparrow$	LPIPS $\downarrow$	
3DGS[17]	30.99	0.926	0.199	24.24	0.705	0.283	27.24	0.803	0.246	19 min
SuGaR[43]	29.44	0.911	0.216	22.76	0.631	0.349	26.06	0.771	0.283	2h
2DGS[1]	25.38	0.811	0.282	22.89	0.762	0.304	24.73	0.877	0.190	24 min
GEF	28.52	0.901	0.183	25.26	0.783	0.177	24.95	0.931	0.08	53 min

Table 4: **Quantitative comparison of geometry reconstruction on the DTU Dataset[48].** The Chamfer Distance error of different methods is reported. The proposed method achieves the best performance among all explicit Gaussian Splatting-based methods, producing comparable accuracy as Neuralangelo. The method is compared with other Gaussian Splatting methods under different resolutions. Methods with and without "(full resolution)" are trained under full resolution and half resolution respectively. Recent ISPRS evaluations[47] show traditional photogrammetry still outperforms neural methods in challenging aerial scenarios, motivating our hybrid entropy-geometric approach.

		24	37	40	55	63	65	69	83	97	105	106	110	114	118	122	Mean	Time
Implicit	NeRF[9]	1.90	1.60	1.85	0.58	2.28	1.27	1.47	1.67	2.05	1.07	0.88	2.53	1.06	1.15	0.96	1.49	> 12h
	VolSDF[49]	1.14	1.26	0.81	0.49	1.25	0.70	0.72	1.29	1.18	0.70	0.66	1.08	0.42	0.61	0.55	0.86	> 12h
	NeuS[29]	1.00	1.37	0.93	0.43	1.10	0.65	0.57	1.48	1.09	0.83	0.52	1.20	0.35	0.49	0.54	0.84	> 12h
	Neuralangelo[50]	0.37	0.72	0.35	0.35	0.87	0.54	0.53	1.29	0.97	0.73	0.47	0.74	0.32	0.41	0.43	0.61	> 12h
Explicit	3DGS[17]	2.14	1.53	2.08	1.68	3.49	2.21	1.43	2.07	2.22	1.75	1.79	2.55	1.53	1.52	1.50	1.96	5.2 min
	SuGaR[43]	1.47	1.33	1.13	0.61	2.25	1.71	1.15	1.63	1.62	1.07	0.79	2.45	0.98	0.88	0.79	1.33	52 min
	2DGS[1]	0.53	0.84	0.39	0.37	1.33	1.23	0.96	1.35	1.29	0.81	0.72	1.62	0.40	0.74	0.51	0.87	8.9 min
	GOF[34]	0.52	0.85	0.50	0.40	1.38	1.05	0.96	1.31	1.35	0.80	0.82	0.86	0.47	0.62	0.46	0.82	55 min
	GEF	0.41	0.69	0.33	0.36	0.80	0.85	0.68	1.28	1.27	0.73	0.64	0.86	0.32	0.64	0.43	0.64	23 min

The geometric accuracy of the joint entropy field method is assessed on the DTU dataset [48] (15 object-centric scenes) and the Tanks and Temples (T&T) dataset [51]. For DTU, Chamfer Distance (lower is better) is reported to measure surface accuracy. For T&T, the F1 score is used to evaluate reconstruction quality and training time is reported to assess efficiency. Baselines include NeRF-based methods (NeRF [9], VolSDF [49], NeuS [29], Neuralangelo [50]) and Gaussian Splatting-based methods (3DGS [17], SuGaR [43], 2DGS [1], GOF [34]). Qualitative comparisons in Figures 8, 10, and 9 show that the method produces smoother and more detailed surfaces than 2DGS and SuGaR, particularly in regions with thin structures or high curvature. Since scanned ground-truth geometry for the ISPRS and DJI datasets is not available, surface reconstruction on these datasets is evaluated only using qualitative visual comparisons.

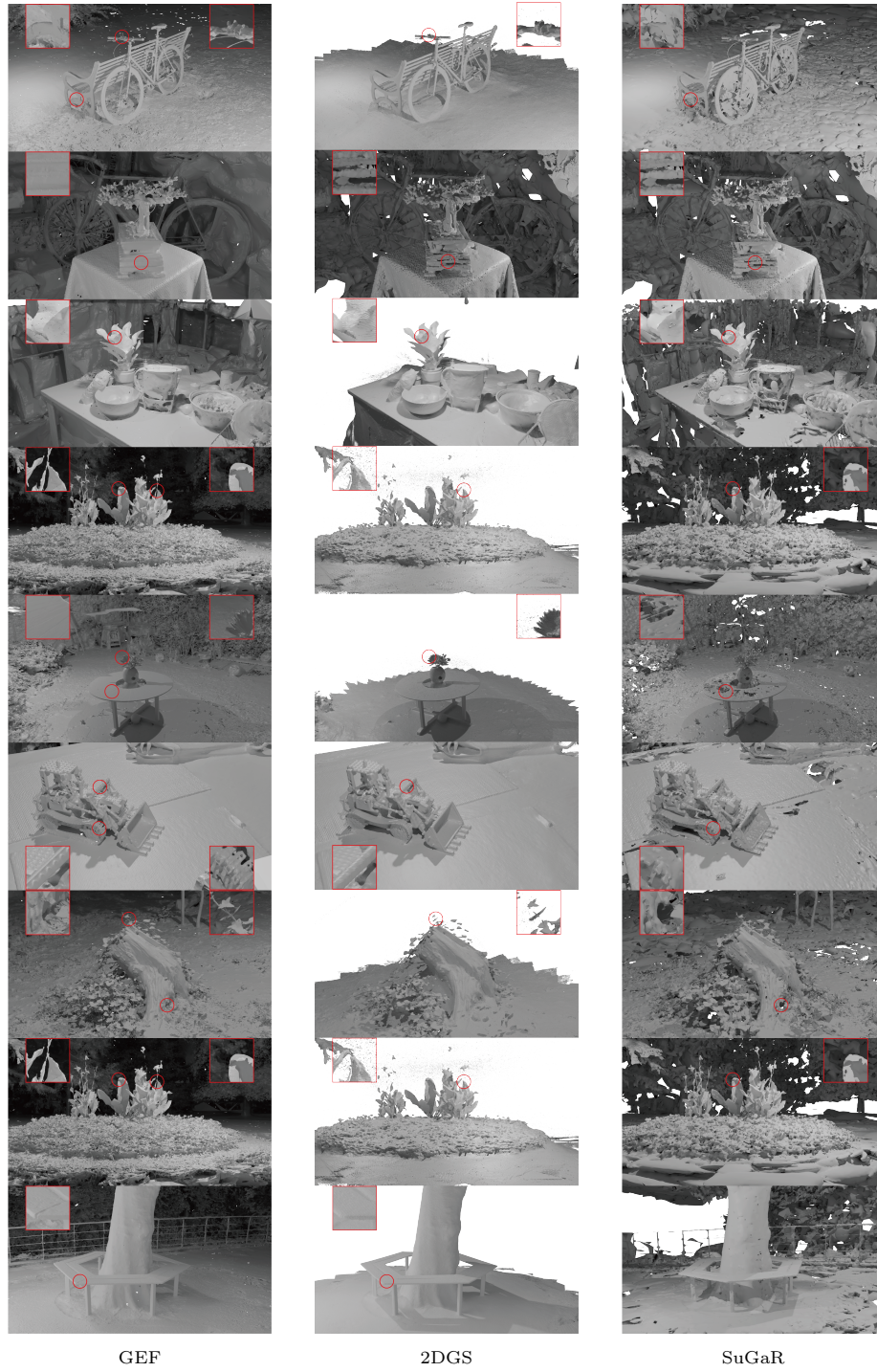


Figure 8: **High-quality surface reconstruction results on the Mip-NeRF 360 dataset.** Incorporating multi-scale entropy effectively guides the reconstruction of fine-grained scene details by regulating the distribution of Gaussian primitives.



Figure 9: **High-quality surface reconstruction results on the T&T dataset.** The figure presents an overview of the reconstructed surfaces, demonstrating the effectiveness of the proposed method.

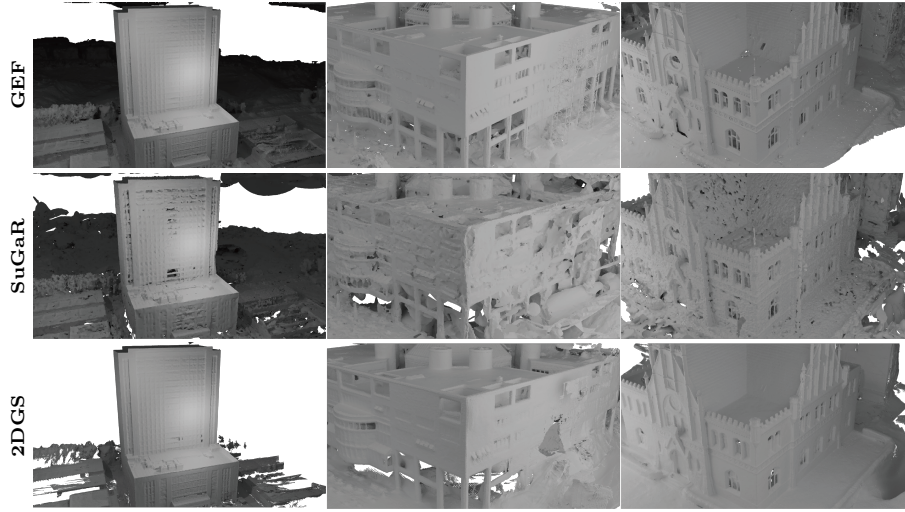


Figure 10: **High-quality surface reconstruction results on the ISPRS dataset and DJI dataset.** Our method addresses geometric consistency challenges identified in recent ISPRS benchmarks [46] for UAV reconstruction applications.

#### 4.3. Ablations and Robustness

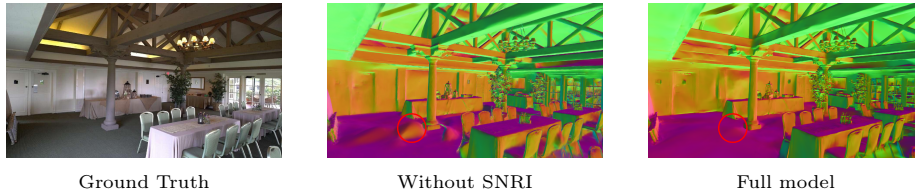


Figure 11: Qualitative comparison of ablation studies. (a) Ground Truth input image. (b) Reconstruction without sparsity constraint component showing significant quality degradation. (c) Full model reconstruction demonstrating superior surface detail preservation and geometric accuracy.

The entropy-based framework is validated through systematic ablation studies. The results demonstrate hierarchical component importance that directly corresponds to the theoretical principles. **Entropy-regularized sparsity constraint:** Removing sparsity constraint causes the most severe

Table 5: **Quantitative results on the T&T dataset [51]**. The F1 score and training time are reported.

Scene	NeuS	Neuralangelo	3DGS	2DGS	SuGaR	GOF	GEF
Barn	0.29	0.70	0.13	0.45	0.14	0.51	0.48
Caterpillar	0.29	0.24	0.08	0.36	0.08	0.41	0.35
Courthouse	0.17	0.13	0.09	0.28	0.08	0.28	0.25
Ignatius	0.83	0.89	0.09	0.50	0.33	0.68	0.75
Meetingroom	0.24	0.32	0.01	0.18	0.15	0.28	0.27
Truck	0.45	0.48	0.19	0.48	0.43	0.58	0.56
Mean	0.38	0.50	0.09	0.32	0.19	0.46	0.44
Time	>24h	>24h	7.9 min	15.5 min	>1h	>1h	50 min

degradation (F1: 0.44→0.37, 15.9% drop), confirming that proper redundancy assessment is crucial for achieving low-entropy surface configurations. **Image Entropy Guidance:** Disabling adaptive weighting reduces F1 score by 9.1%, validating that uniform constraints break spatial coherence across regions of varying complexity. **Multi-Scale Alignment:** The 4.5% F1 score degradation confirms that geometric complexity varies across scales, requiring adaptive entropy constraints for hierarchical detail preservation. **Key Insights:** (1) F1 score shows higher sensitivity than photometric metrics, confirming the framework primarily benefits geometric accuracy. (2) Non-additive performance gains demonstrate synergistic component interaction rather than independent contributions. (3) Each ablation failure mode directly corresponds to violations of the theoretical principles, providing empirical validation for the information-theoretic method.

Table 6: **Ablation study on the T&T dataset.**

Setting	F1 score ↑	PSNR ↑	SSIM ↑	LPIPS ↓
w/o sparsity constraint	0.37	23.51	0.850	0.196
w/o ImageEntropy	0.40	24.62	0.865	0.170
w/o Multi-Scale	0.42	25.22	0.872	0.157
Full model	0.44	25.89	0.870	0.150

To evaluate robustness to realistic sensor noise, the Mip-NeRF 360 dataset is augmented with synthetic noise using a mixed noise generator. The noise model, termed realistic sensor, combines shot noise (scale=1.3), Gaussian noise (mean=0, std=12), dark current noise (intensity=6), and impulse noise (salt and pepper probability=0.008), simulating typical sensor imperfections in drone-captured imagery. Additional presets—light, medium, and heavy—escalate noise intensities for graded evaluation (e.g., heavy includes Gaussian std=25, impulse prob=0.02). Noise is applied to all training images in the Mip-NeRF



360 dataset, and the noisy dataset is processed using the GEF framework with the same optimization settings as the clean data experiments.

Table 7: **Performance under varying noise levels on Mip-NeRF 360.**

Noise Level	Gaussian Std ( $\sigma$ )	Proposed (GEF)			2DGS (Baseline)		
		PSNR $\uparrow$	SSIM $\uparrow$	LPIPS $\downarrow$	PSNR $\uparrow$	SSIM $\uparrow$	LPIPS $\downarrow$
None (Clean)	0	27.40	0.855	0.136	26.93	0.796	0.297
Noisy light	8	26.53	0.826	0.157	27.08	0.801	0.206
Noisy medium	15	25.25	0.710	0.156	25.41	0.774	0.214
Noisy heavy	25	22.08	0.739	0.192	22.07	0.774	0.235
Realistic Sensor	12	26.48	0.809	0.161	26.27	0.786	0.211

Table 7 demonstrates that GEF consistently outperforms 2DGS across all noise levels, with smaller degradations (e.g., under realistic sensor noise: SSIM 0.855 $\rightarrow$ 0.809 vs. 0.796 $\rightarrow$ 0.786; LPIPS 0.136 $\rightarrow$ 0.161 vs. 0.297 $\rightarrow$ 0.211). This robustness is attributed to the entropy regularization framework, which suppresses noise-induced primitive aliasing by minimizing configurational entropy (Eq. (5)). The adaptive weighting in multi-scale entropy alignment (Eq. (13)) further mitigates noise impact by reducing the influence of high-entropy regions, even at heavy noise where GEF preserves better structural fidelity.

#### 4.4. Hyperparameter Sensitivity Analysis

To provide practical guidance for parameter selection and demonstrate the robustness of the GEF framework, a comprehensive sensitivity analysis is conducted on two critical hyperparameters: the delayed update interval  $N$  for entropy components and the temperature parameter  $\beta$  for competitive multi-scale weighting.

**Delayed Update Interval ( $N$ ).** The hyperparameter  $N$  controls the frequency of entropy map updates relative to model parameter optimization, utilizing the temporal scale separation between fast parameter evolution and slow configurational entropy distribution.

Table 8: **Sensitivity analysis of delayed update interval  $N$  on DTU dataset.**

Update Interval $N$	Training Time (min)	PSNR $\uparrow$	CD $\downarrow$
1 (every iteration)	52	34.20	0.68
5	33	34.81	0.63
10	28	34.77	0.64
20	23	34.69	0.64
50	20	34.55	0.65
100	18	34.37	0.71

Table 8 reveals a clear trade-off between computational efficiency and reconstruction quality. Smaller update intervals (e.g.,  $N = 1$ ) provide the most stable optimization but incur significant computational overhead due to frequent

entropy recalculation. As  $N$  increases, training time decreases proportionally, with minimal quality degradation up to  $N = 20$ . However, excessively large intervals ( $N \geq 50$ ) lead to instability in entropy constraints, causing oscillations in the loss function and degraded final quality. The optimal balance is achieved at  $N = 10$ -20, offering 3-4 $\times$  speedup while maintaining performance within 1% of the baseline.

**Competitive Weighting Temperature ( $\beta$ ).** The temperature parameter  $\beta$  in Eq. (13) controls the sharpness of competition between different scales in the multi-scale entropy alignment. A higher  $\beta$  value enforces stronger scale specialization, while lower values promote smoother weight distribution across scales.

Table 9: **Sensitivity analysis of temperature parameter  $\beta$  on DTU dataset.**

Temperature $\beta$	PSNR $\uparrow$	SSIM $\uparrow$	LPIPS $\downarrow$
1.0	33.80	0.903	0.141
3.0	34.20	0.928	0.122
6.0 (default)	34.64	0.950	0.100
8.0	34.33	0.945	0.106
10.0	34.28	0.912	0.132
12.0	34.03	0.922	0.118

The analysis in Table 9 demonstrates that  $\beta = 6.0$  provides the optimal balance between scale specialization and training stability. Lower values ( $\beta < 3.0$ ) result in insufficient competition, leading to diffuse weight distributions where multiple scales simultaneously influence the same region, reducing the effectiveness of adaptive entropy constraints. Higher values ( $\beta > 10.0$ ) create overly sharp competition that can cause training instability due to aggressive gradient changes in the softmax function, particularly in regions with similar entropy values across scales.

**Practical Recommendations.** Based on the comprehensive sensitivity analysis, we provide the following guidelines for practical deployment of GEF:

- **Update interval  $N$ :** Use  $N = 10$ -20 for most applications to balance efficiency and quality. Consider  $N = 5$  for high-precision requirements where computational resources are abundant.
- **Temperature  $\beta$ :** The default  $\beta = 6.0$  works well across diverse scenes. Reduce to  $\beta = 4.0$ -5.0 for scenes with gradual scale transitions, or increase to  $\beta = 8.0$  for scenes with clear scale separation.
- **Adaptive strategies:** For large-scale scenes with varying complexity, consider spatially-varying  $\beta$  values that adapt to local entropy gradients.

**Neighborhood Construction.** Local neighborhoods  $\Omega_k$  are defined using  $K$ -nearest neighbors with  $K \in [25, 64]$ , where the exact value is adaptively determined by local primitive density. Two key properties make this choice robust:

(1) *Overlap-induced information propagation:* Since  $\Omega_i \cap \Omega_j \neq \emptyset$  for nearby primitives, entropy constraints diffuse through multi-hop connections. Over 10,000 iterations (20,000-30,000), even moderate  $K = 25$  yields effective communication range  $\gg K$ .

(2) *One-time computation suffices:* Neighborhood topology is fixed at iteration 20,000, after geometric regularization establishes surface alignment.

The hyperparameter sensitivity analysis confirms that GEF exhibits robust performance across a wide range of parameter settings, with clear optimal regions that provide practical guidance for deployment while maintaining the theoretical guarantees of the entropy-based framework.

## 5. CONCLUSION

This work introduces Gaussian Entropy Fields (GEF), an entropy-based framework that reformulates surface reconstruction in 3D Gaussian Splatting as an information-theoretic optimization problem. By minimizing neighborhood entropy under photometric and geometric regularization, GEF drives Gaussian primitives toward surface-consistent configurations, where a small number of dominant primitives define the geometry and redundant components are suppressed. This approach achieves surface reconstruction without the need for additional explicit surface parameterizations. Extensive experiments demonstrate competitive geometric precision on DTU (Chamfer Distance: 0.64) and T&T (F1 score: 0.44), alongside superior rendering quality on Mip-NeRF 360 (SSIM: 0.855, LPIPS: 0.136). Unlike traditional geometric constraints that often degrade photometric quality, our method allows surface properties to emerge naturally while maintaining rendering fidelity. The method shows robust performance across diverse scenarios from dense indoor scenes to sparse aerial captures.

### Limitations and Future Work.

While GEF generally improves geometric consistency and robustness, several failure modes remain. First, in extremely thin or low-texture structures, the entropy-based sparsification may become overly aggressive, leading to partial surface disappearance or over-pruning of primitives. Second, highly specular or view-dependent surfaces can produce unstable opacity profiles, which weaken the assumption of locally consistent entropy and may result in fragmented or floating surfaces. Third, under very sparse-view scenarios, the SNRI measure may misinterpret missing coverage as redundancy, causing valid primitives to collapse prematurely. These failure cases indicate that GEF still depends on sufficient texture richness, moderate viewpoint coverage, and stable opacity cues.

Future work could explore dynamic entropy computation, reflectance-aware entropy modeling, and uncertainty-driven neighborhood construction for more challenging scenarios such as extremely sparse inputs or dynamic scenes.



## References

- [1] B. Huang, Z. Yu, A. Chen, A. Geiger, S. Gao, 2d gaussian splatting for geometrically accurate radiance fields, in: ACM SIGGRAPH 2024 Conference Papers, 2024, pp. 1–11.
- [2] V. Kolmogorov, R. Zabih, Computing visual correspondence with occlusions using graph cuts, in: Proc. IEEE Int. Conf. on Computer Vision (ICCV), Vol. 2, IEEE, 2001, pp. 508–515.
- [3] E. Rupnik, M. Pierrot Deseilligny, A. Delorme, 3d reconstruction from multi-view vhr-satellite images in micmac, ISPRS Journal of Photogrammetry and Remote Sensing 139 (2018) 201–211. [doi:10.1016/j.isprsjprs.2018.02.012](https://doi.org/10.1016/j.isprsjprs.2018.02.012).
- [4] M. Kazhdan, M. Bolitho, H. Hoppe, Poisson surface reconstruction, in: Proc. Eurographics Symp. on Geometry Processing (SGP), Vol. 7, Eurographics, 2006.
- [5] S. Paris, F. X. Sillion, L. Quan, A surface reconstruction method using global graph cut optimization, International Journal of Computer Vision 66 (2006) 141–161.
- [6] F. Rottensteiner, G. Sohn, M. Gerke, J. D. Wegner, U. Breitkopf, J. Jung, Results of the isprs benchmark on urban object detection and 3d building reconstruction, ISPRS journal of photogrammetry and remote sensing 93 (2014) 256–271.
- [7] M. Bleyer, C. Rhemann, C. Rother, Patchmatch stereo: Stereo matching with slanted support windows, in: Proc. British Machine Vision Conference (BMVC), Vol. 11, BMVA, 2011, pp. 1–11.
- [8] M. Kazhdan, H. Hoppe, Screened poisson surface reconstruction, ACM Transactions on Graphics (TOG) 32 (3) (2013) 1–13.
- [9] B. Mildenhall, P. P. Srinivasan, M. Tancik, J. T. Barron, R. Ramamoorthi, R. Ng, Nerf: Representing scenes as neural radiance fields for view synthesis, Communications of the ACM 65 (1) (2021) 99–106.
- [10] H. Matsuki, R. Murai, P. H. Kelly, A. J. Davison, Gaussian splatting slam, in: Proceedings of the IEEE/CVF Conference on Computer Vision and Pattern Recognition (CVPR), 2024, pp. 18039–18048.
- [11] N. Deng, Z. He, J. Ye, B. Duinkharjav, P. Chakravarthula, X. Yang, Q. Sun, Fov-nerf: Foveated neural radiance fields for virtual reality, IEEE Transactions on Visualization and Computer Graphics 28 (11) (2022) 3854–3864.

- [12] Y. Cai, Y. Liang, J. Wang, A. Wang, Y. Zhang, X. Yang, Z. Zhou, A. Yuille, Radiative gaussian splatting for efficient x-ray novel view synthesis, in: European Conference on Computer Vision (ECCV), Springer, 2024, pp. 283–299.
- [13] S. J. Garbin, M. Kowalski, M. Johnson, J. Shotton, J. Valentin, Fastnerf: High-fidelity neural rendering at 200fps, in: Proceedings of the IEEE/CVF International Conference on Computer Vision (ICCV), 2021, pp. 14346–14355.
- [14] R. Martin-Brualla, N. Radwan, M. S. Sajjadi, J. T. Barron, A. Dosovitskiy, D. Duckworth, Nerf in the wild: Neural radiance fields for unconstrained photo collections, in: Proceedings of the IEEE/CVF Conference on Computer Vision and Pattern Recognition (CVPR), 2021, pp. 7210–7219.
- [15] I. Colomina, P. Molina, Unmanned aerial systems for photogrammetry and remote sensing: A review, *ISPRS Journal of Photogrammetry and Remote Sensing* 92 (2014) 79–97. [doi:10.1016/j.isprsjprs.2014.02.013](https://doi.org/10.1016/j.isprsjprs.2014.02.013).
- [16] L. Barazzetti, F. Banfi, R. Brumana, G. Gusmeroli, M. Previtali, G. Schiantarelli, Cloud-to-bim-to-fem: Structural simulation with accurate historic bim from laser scans, *Simulation modelling practice and theory* 57 (2015) 71–87.
- [17] B. Kerbl, G. Kopanas, T. Leimkühler, G. Drettakis, 3d gaussian splatting for real-time radiance field rendering, *ACM Transactions on Graphics (TOG)* 42 (4) (2023) 139:1–139:14.
- [18] G. Vogiatzis, C. H. Esteban, P. H. Torr, R. Cipolla, Multiview stereo via volumetric graph-cuts and occlusion robust photo-consistency, *IEEE Transactions on Pattern Analysis and Machine Intelligence* 29 (12) (2007) 2241–2246.
- [19] Y. Furukawa, J. Ponce, Accurate, dense, and robust multiview stereopsis, *IEEE Transactions on Pattern Analysis and Machine Intelligence* 32 (8) (2009) 1362–1376.
- [20] Y. Liao, X. Zhang, N. Huang, C. Fu, Q. Cao, Z. Xu, X. Xiong, S. Cai, . . . , High completeness multi-view stereo for dense reconstruction of large-scale urban scenes, *ISPRS Journal of Photogrammetry and Remote Sensing* 209 (5) (2024) 173–196. [doi:10.1016/j.isprsjprs.2024.01.018](https://doi.org/10.1016/j.isprsjprs.2024.01.018).
- [21] Y. Yao, Z. Luo, S. Li, T. Fang, L. Quan, Mvsnet: Depth inference for unstructured multi-view stereo, in: European Conference on Computer Vision (ECCV), Springer, 2018, pp. 767–783.
- [22] F. Wang, S. Galliani, C. Vogel, P. Speciale, M. Pollefeys, Patchmatchnet: Learned multi-view patchmatch stereo, in: Proceedings of the IEEE/CVF Conference on Computer Vision and Pattern Recognition, IEEE, 2021, pp. 14194–14203.

- [23] S. M. Seitz, C. R. Dyer, View morphing, in: Proceedings of the 23rd Annual Conference on Computer Graphics and Interactive Techniques, ACM, 1996, pp. 21–30.
- [24] M. Levoy, P. Hanrahan, Light field rendering, in: Seminal Graphics Papers: Pushing the Boundaries, Volume 2, ACM, 2023, pp. 441–452.
- [25] T. Zhou, R. Tucker, J. Flynn, G. Fyffe, N. Snavely, Stereo magnification: Learning view synthesis using multiplane images, arXiv preprint arXiv:1805.09817 (2018).
- [26] V. Sitzmann, J. Thies, F. Heide, M. Nießner, G. Wetzstein, M. Zollhofer, Deepvoxels: Learning persistent 3d feature embeddings, in: Proceedings of the IEEE/CVF Conference on Computer Vision and Pattern Recognition, IEEE, 2019, pp. 2437–2446.
- [27] K. Deng, A. Liu, J.-Y. Zhu, D. Ramanan, Depth-supervised nerf: Fewer views and faster training for free, in: Proceedings of the IEEE/CVF Conference on Computer Vision and Pattern Recognition, IEEE, 2022, pp. 12882–12891.
- [28] C.-H. Lin, W.-C. Ma, A. Torralba, S. Lucey, Barf: Bundle-adjusting neural radiance fields, in: Proceedings of the IEEE/CVF International Conference on Computer Vision, IEEE, 2021, pp. 5741–5751.
- [29] P. Wang, L. Liu, Y. Liu, C. Theobalt, T. Komura, W. Wang, Neus: Learning neural implicit surfaces by volume rendering for multi-view reconstruction, arXiv preprint arXiv:2106.10689 (2021).
- [30] T. Liu, S. Zhang, Z. Li, Y. Sun, et al., A novel entropy-based regularization for nerf to view synthesis in few-shot scenarios, in: Advances in Neural Networks – ISNN 2024, Vol. 14827 of Lecture Notes in Computer Science, 2024, pp. 113–122. doi:10.1007/978-981-97-4399-5\_11.
- [31] W. Luo, B. Zhang, Z. Zhang, Entropy-based training methods for scalable neural implicit sampler, in: Advances in Neural Information Processing Systems (NeurIPS) 36, 2023, main Conference Track.  
URL <https://proceedings.neurips.cc/paper/2023/hash/1646e34971facbcd3727d1dc28ab635-Abstract.html>
- [32] L. Zhang, E. Rupnik, Sparsesat-nerf: Dense depth supervised neural radiance fields for sparse satellite images, ISPRS Annals of the Photogrammetry, Remote Sensing and Spatial Information Sciences X-1/W1-2023 (2023) 895–902. doi:10.5194/isprs-annals-X-1-W1-2023-895-2023.
- [33] J. Liu, J. Gao, S. Ji, C. Zeng, S. Zhang, J. Gong, Deep learning based multi-view stereo matching and 3d scene reconstruction from oblique aerial images, ISPRS Journal of Photogrammetry and Remote Sensing 204 (2023) 42–60. doi:10.1016/j.isprsjprs.2023.10.005.

- [34] Z. Yu, T. Sattler, A. Geiger, Gaussian opacity fields: Efficient adaptive surface reconstruction in unbounded scenes, *ACM Transactions on Graphics (TOG)* 43 (6) (2024) 1–13.
- [35] D. Chen, H. Li, W. Ye, Y. Wang, W. Xie, S. Zhai, N. Wang, H. Liu, H. Bao, G. Zhang, Pgsr: Planar-based gaussian splatting for efficient and high-fidelity surface reconstruction, *IEEE Transactions on Visualization and Computer Graphics* (2024).
- [36] M. Zwicker, H. Pfister, J. Van Baar, M. Gross, Ewa volume splatting, in: *Proceedings Visualization, 2001. VIS'01.*, IEEE, 2001, pp. 29–538.
- [37] D. Huang, R. Qin, A critical analysis of internal reliability for uncertainty quantification of dense image matching in multi-view stereo, *arXiv preprint arXiv:2309.09379* (2023).
- [38] B. Curless, M. Levoy, A volumetric method for building complex models from range images, in: *Proceedings of the 23rd Annual Conference on Computer Graphics and Interactive Techniques*, 1996, pp. 303–312.
- [39] W. E. Lorensen, H. E. Cline, Marching cubes: A high resolution 3d surface construction algorithm, in: *Seminal Graphics: Pioneering Efforts that Shaped the Field*, 1998, pp. 347–353.
- [40] J. T. Barron, B. Mildenhall, M. Tancik, P. Hedman, R. Martin-Brualla, P. P. Srinivasan, Mip-nerf: A multiscale representation for anti-aliasing neural radiance fields, in: *Proceedings of the IEEE/CVF International Conference on Computer Vision*, 2021, pp. 5855–5864.
- [41] P. Hedman, J. Philip, T. Price, J.-M. Frahm, G. Drettakis, G. Brostow, Deep blending for free-viewpoint image-based rendering, *ACM Transactions on Graphics (ToG)* 37 (6) (2018) 1–15.
- [42] T. Müller, A. Evans, C. Schied, A. Keller, Instant neural graphics primitives with a multiresolution hash encoding, *ACM transactions on graphics (TOG)* 41 (4) (2022) 1–15.
- [43] A. Guédon, V. Lepetit, Sugar: Surface-aligned gaussian splatting for efficient 3d mesh reconstruction and high-quality mesh rendering, in: *Proceedings of the IEEE/CVF Conference on Computer Vision and Pattern Recognition (CVPR)*, 2024, pp. 5354–5363.
- [44] F. Nex, M. Gerke, F. Remondino, H.-J. Przybilla, M. Bäumker, A. Zurhorst, [Isprs benchmark for multi-platform photogrammetry](https://doi.org/10.5194/isprsannals-II-3-W4-135-2015), *ISPRS Annals of the Photogrammetry, Remote Sensing and Spatial Information Sciences II-3/W4* (2015) 135–142. [doi:10.5194/isprsannals-II-3-W4-135-2015](https://doi.org/10.5194/isprsannals-II-3-W4-135-2015). URL <https://doi.org/10.5194/isprsannals-II-3-W4-135-2015>

- [45] B. Mildenhall, P. P. Srinivasan, M. Tancik, J. T. Barron, R. Ramamoorthi, R. Ng, [Nerf synthetic dataset](#), Project Website, part of the NeRF project, containing 8 synthetic scenes created with Blender (2020).  
URL <https://www.matthewtancik.com/nerf/synthetic/>
- [46] F. Nex, F. Remondino, E. Rupnik, et al., [Benchmarking uav photogrammetry and computer vision: A review of isprs datasets and competitions](#), ISPRS Journal of Photogrammetry and Remote Sensing 203 (2023) 76–92.  
[doi:10.1016/j.isprsjprs.2023.05.011](#).  
URL <https://doi.org/10.1016/j.isprsjprs.2023.05.011>
- [47] T. Haitz, S. Hackstein, P. Reinartz, [The potential of neural radiance fields and 3d gaussian splatting for 3d reconstruction from aerial imagery](#), ISPRS Annals of the Photogrammetry, Remote Sensing and Spatial Information Sciences X-2-2024 (2024) 113–120. [doi:10.5194/isprs-annals-X-2-2024-113-2024](#).  
URL <https://doi.org/10.5194/isprs-annals-X-2-2024-113-2024>
- [48] R. Jensen, A. Dahl, G. Vogiatzis, E. Tola, H. Aanæs, Large scale multi-view stereopsis evaluation, in: Proceedings of the IEEE Conference on Computer Vision and Pattern Recognition, IEEE, 2014, pp. 406–413.
- [49] L. Yariv, J. Gu, Y. Kasten, Y. Lipman, Volume rendering of neural implicit surfaces, Advances in Neural Information Processing Systems 34 (2021) 4805–4815.
- [50] Z. Li, T. Müller, A. Evans, R. H. Taylor, M. Unberath, M.-Y. Liu, C.-H. Lin, Neuralangelo: High-fidelity neural surface reconstruction, in: Proceedings of the IEEE/CVF Conference on Computer Vision and Pattern Recognition, 2023, pp. 8456–8465.
- [51] A. Knapitsch, J. Park, Q.-Y. Zhou, V. Koltun, Tanks and temples: Benchmarking large-scale scene reconstruction, ACM Transactions on Graphics (TOG) 36 (4) (2017) 1–13.